Fuel Injection Model for Euler-Euler and Euler-Lagrange Large-Eddy Simulations of an evaporating spray inside an aeronautical combustor

M. Sanjosé[a], J.M. Senoner[a], F. Jaegle[a], B. Cuenot[a], S. Moreau[b], T. Poinsot[c]

[a] *CERFACS - CFD Team, 42 avenue Gaspard Coriolis, 31057 Toulouse Cedex 01, France*
[b] *Université de Sherbrooke, GAUS, Département de Génie Mécanique, Sherbrooke J1K2R1, QC Canada*
[c] *Institut de Mécanique des Fluides de Toulouse, Allée du Professeur Camille Soula, 31400 Toulouse, France*

Abstract

Large-Eddy Simulations (LES) of an evaporating two-phase flow in an experimental burner are investigated. Two different numerical approaches for the simulation of the dispersed phase are coupled to the same gaseous solver: a mesoscopic Eulerian method and a Lagrangian particle tracking technique. The spray is represented by a single droplet size owing to the locally monodisperse formulation of the employed mesoscopic Eulerian approach. Both approaches use the same drag and evaporation models. They do not take into account the atomization process and a simplified injection model is applied instead. The presented methodology, referred as FIM-UR (Fuel Injection Method by Upstream Reconstruction) defines injection profiles for the monodisperse spray produced by a pressure-swirl atomizer. It is designed so as to ensure similar spray characteristics for both approaches and allows for a direct comparison between them. After a validation of the purely

Email address: marlene.sanjose@gmail.com (M. Sanjosé)

gaseous flow in the burner, liquid-phase dynamics and droplet dispersion are qualitatively and quantitatively evaluated for the Eulerian and Lagrangian simulations. Results obtained for both approaches are in very good agreement and compare reasonably with experiments, indicating that simplified injection methods are appropriate for the simulation of realistic combustor geometries.
Keywords: Large eddy simulation, liquid injection, Euler-Euler mesoscopic approach, Euler-Lagrange approach

1. Introduction

Large-Eddy simulation (LES) has shown its potential for single-phase reacting flows in aeroengine combustors (Mahesh et al., 2004; Selle et al., 2004) and is being extended to two-phase reacting flows where the prediction of the combustion mechanisms depends on the quality of the fuel air mixing into the combustion chamber. Two-phase flow LES are able to reproduce the droplet dispersion (Boivin et al., 2000; Apte et al., 2003; Riber et al., 2009) and evaporation (Boileau et al., 2008b; Patel and Menon, 2008; Apte et al., 2009) mechanisms which influence the fuel air mixing. However, two-phase flow LES are limited to dispersed sprays and do not take into account primary atomization. As a result, these two-phase flow simulations rely on a detailed characterization of the atomized spray close to injection.

The fuel spray pattern is produced by the atomization of the liquid fuel into small droplets. In aeroengine applications, the atomization process is enhanced by pressure-swirl atomizers, extensively studied and described in the literature (Lefebvre, 1989; Bayvel and Orzechowski, 1993). Even for

pressure-swirl atomizers having the simplest internal geometry (*simplex*), the spray pattern is influenced by several design parameters and local turbulence parameters (Taylor, 1948; Jones and Whitelaw, 1982; Rizk and Lefebvre, 1983).

To describe the dispersed phase, most LES codes use an Euler/Lagrange (EL) method in which the gas phase is solved using an Eulerian method while the particles are tracked in a Lagrangian framework (Sankaran and Menon, 2002; Patel and Menon, 2008; Apte et al., 2009). An alternative approach to describe the dispersed phase is the Euler/Euler (EE) method in which both phases are solved using an Eulerian description. In this approach the dispersed phase is considered as a continuum built from the ensemble averaging of particle realizations (Février et al., 2005; Kaufmann et al., 2008; Boileau et al., 2008a; Riber et al., 2009). In the EE approach, both phases are solved on the same mesh grid with the same discretization schemes, whereas in the EL approach, quantities needed for the coupling between phases have to be interpolated at the droplet position or distributed at the mesh nodes. In the present study, the two approaches, implemented into the same LES gas solver, are compared to describe dispersed two-phase flows in a real gas turbine geometry.

Numerical simulations of the atomization process are a recent research topic. They rely on the development of specific numerical tools, such as interface tracking or capturing techniques (Menard et al., 2007; Desjardins et al., 2008), which require a high level of precision and remain limited in terms of Reynolds number and geometrical complexity. They are not yet suitable for the simulation of the real injection in an actual combustion chamber.

The present study describes an alternative and simplified methodology to build the size and velocity distributions of the droplets at injection without solving primary atomization. The proposed methodology called FIM-UR, for *Fuel Injection Method by Upstream Reconstruction*, allows to specify the boundary conditions for fuel injection by pressure-swirl atomizer for both EE and EL methods within the same framework.

The paper is organized as follows. First the LES equations and models for two-phase flows are recalled, including both the Eulerian and Lagrangian formulations for the dispersed phase. Then the FIM-UR methodology is presented: the boundary conditions for both the EL and the EE approach are derived from input parameters and balance equations. The third part describes the application to an experimental configuration. Results are analyzed in terms of validation against experimental data, evaluation of the FIM-UR model and comparison of the EL and EE methods.

2. System equations

2.1. Gas phase

The unstructured LES code AVBP explicitly solves the filtered compressible Navier-Stokes equations:

$$\frac{\partial \overline{\rho}\widetilde{u_i}}{\partial t} + \frac{\partial \overline{\rho}\widetilde{u_i}\widetilde{u_j}}{\partial x_j} = -\frac{\partial}{\partial x_j}[\overline{p}\delta_{ij} - \overline{\tau}_{ij} - \overline{\tau}_{ij}^{sgs})] + \overline{\dot{s}}_{mo,i} \tag{1}$$

$$\frac{\partial \overline{\rho}E}{\partial t} + \frac{\partial \overline{\rho}\widetilde{E}\widetilde{u_j}}{\partial x_j} = -\frac{\partial}{\partial x_j}[\overline{u_i(p\delta_{ij} - \tau_{ij})} + \overline{q}_j + \overline{q}_j^{sgs}] + \overline{\dot{s}}_{en} \tag{2}$$

$$\frac{\partial \overline{\rho}\widetilde{Y_k}}{\partial t} + \frac{\partial \overline{\rho}\widetilde{Y}_k\widetilde{u_j}}{\partial x_j} = \frac{\partial}{\partial x_j}[\overline{J_{j,k}} - \overline{J}_{j,k}^{sgs}] + \overline{\dot{s}}_{ms,k} \qquad \text{for k=1,N} \tag{3}$$

$\overline{\cdot}$ states for the Reynolds spatial filtering and $\widetilde{\cdot}$ states for the Favre spatial filtering: $\overline{\rho f} = \overline{\rho}\widetilde{f}$. Einstein's summation convention is applied over repeated indices and δ_{ij} denotes the Kronecker symbol. The inter-phase exchange terms of momentum, energy and mass respectively, $\overline{\dot{s}}_{mo,i}$, $\overline{\dot{s}}_{en}$ and $\overline{\dot{s}}_{ms,k}$, will be detailed in subsection 2.3.

$\overline{\tau}_{ij}$ stands for the laminar filtered stress tensor. The diffusive species flux $\overline{J_{i,k}}$ is evaluated with the Hirschfelder and Curtis approximation (Hirschfelder et al., 1964), a correction term being added to ensure mass conservation (Poinsot and Veynante, 2001). The heat flux $\overline{q}_j$ takes into account temperature diffusion as well as enthalpy flux due to differential species diffusion following Fourier's law. For the sub-grid unclosed terms, the classical eddy-viscosity assumption is made:

$$\overline{\tau}_{ij}^{sgs} = \overline{\rho}(\widetilde{u_i u_j} - \widetilde{u}_i\widetilde{u}_j) \approx 2\overline{\rho}\nu_t\left(\widetilde{S_{ij}} - \frac{1}{3}\widetilde{S_{kk}}\delta_{ij}\right) \tag{4}$$

and similarly for $\overline{J}_{j,k}^{sgs}$ and $\overline{q}_j^{sgs}$:

$$\overline{J}_{j,k}^{sgs} = \overline{\rho}(\widetilde{u_j Y_k} - \widetilde{u}_j\widetilde{Y}_k) \approx -\overline{\rho}\left(D_t\frac{W_k}{W}\frac{\partial\widetilde{X_k}}{\partial x_j} - \widetilde{Y}_k\widetilde{V_j^c}\right) \tag{5}$$

$$\overline{q}_j^{sgs} = \overline{\rho}(\widetilde{u_j E} - \widetilde{u}_j\widetilde{E}) \approx -\lambda_t\frac{\partial\widetilde{T}}{\partial x_j} + \sum_{k=1}^{N}\overline{J}_{j,k}^{sgs}\widetilde{h}_{s,k} \tag{6}$$

The turbulent viscosity is computed with the Wall Adapting Local Eddy-viscosity model (Nicoud and Ducros, 1999), which recovers the right scaling of turbulent viscosity close to solid boundaries and yields reduced damping in zones of pure shear compared to the standard Smagorinsky model (Smagorinsky, 1963). The turbulent diffusive coefficients D_t and λ_t are computed from the turbulent viscosity and turbulent Schmidt and Prandtl numbers equal to 0.6: $D_t = \nu_t/Sc_t$ and $\lambda_t = \overline{\rho}\nu_t\overline{C_p}/Pr_t$.

Equations (1)-(3) are numerically solved with an optimized Two-step Taylor-Galerkin scheme (TTGC) which achieves third order accuracy in time and space for convective terms (Colin and Rudgyard, 2000). Inlet and outlet boundary condition treatment relies on one-dimensional formulation for non-reflecting characteristic boundary conditions for viscous flows (Poinsot and Lele, 1992).

2.2. Dispersed liquid phase

For both approaches, it is assumed that the density of the droplets is much larger than that of the carrier fluid, the droplets are dispersed and collisions between them are negligible, the droplets are much smaller than the LES filter width, droplet deformation effects are small, motion due to shear is negligible and gravitational effects are not significant compared to drag. The governing equations of motion for the dispersed liquid-phase of the Euler-Lagrange and the Euler-Euler formalisms are presented in the two next sections.

2.2.1. Euler-Lagrange approach

Under the previous assumptions, the Lagrangian equations governing the droplet motion read:

$$\frac{dx_{p,i}}{dt} = u_{p,i} \quad \text{and} \quad \frac{du_{p,i}}{dt} = \frac{f_{p,i}}{m_p} \tag{7}$$

where m_p is the mass of the droplet, $\mathbf{x}_p$ the position of the droplet centroid and $\mathbf{u}_p$ the droplet velocity. $\mathbf{f}_p$ is the drag force acting upon the droplet.

When dealing with evaporating droplets, equations for the droplet mass

m_p and temperature T_p must also be solved:

$$\frac{dm_p}{dt} = \dot{m}_p \quad \text{and} \quad \frac{dT_p}{dt} = \frac{-1}{m_p C_{p,l}} \phi_p^c \tag{8}$$

where $\dot{m}_p$ is the evaporating mass rate, $C_{p,l}$ the specific heat of the liquid and ϕ_p^c the conductive heat flux on the liquid side at the droplet surface.

For time advancement, the Lagrangian solver uses a two-step Runge-Kutta method coupled to two iterations of the gaseous solver, so that $\Delta t_p = 2\Delta t_g$.

2.2.2. Euler-Euler approach

The Eulerian approach describes the dispersed phase with ensemble average of the droplet properties over a given set of liquid-phase realizations, conditioned on one gas-phase realization and denoted $\langle \cdot | \mathcal{H}_f \rangle_l$ or $\breve{\cdot}$ to lighten equations. The continuous averaged properties called the mesoscopic quantities are for a *mono-disperse* evaporating spray: the droplet number density, the liquid volume fraction, the mesoscopic velocity and the mesoscopic enthalpy. Locally the spray is described by a single diameter d defined by $\breve{\alpha}_l = \breve{n}_l \, \pi d^3/6$.

The discrete drop velocity $\mathbf{u}_p$ may be separated into an Eulerian part, the mesoscopic velocity $\breve{\mathbf{u}}_l$ and a Lagrangian random part, the random uncorrelated velocity $\mathbf{u}_p''$ (Février et al., 2005):

$$\mathbf{u}_p = \breve{\mathbf{u}}_l + \mathbf{u}_p'' \tag{9}$$

This random motion leads to an isotropic redistribution of droplets which is enhanced in zones of shear and compressibility effects of the mesoscopic motion (Simonin et al., 2002). In the considered Eulerian approach, this

effect is taken into account by solving a transport equation for the associated kinetic energy $\delta\breve{\theta}_l$.

By analogy with the gas phase Favre filtering, a LES filter is applied to the mesoscopic equations $\overline{\breve{\alpha}_l \breve{f}_l} = \overline{\alpha}_l \widehat{f}_l$ where $\overline{\alpha}_l$ is the spatially filtered liquid volume fraction. It is assumed that the subgrid velocity accounts only for the mesoscopic motion. The final set of filtered equations for the dispersed phase is summarized below (Moreau et al., 2010).

$$\frac{\partial \overline{n}_l}{\partial t} + \frac{\partial \overline{n}_l \widehat{u}_{l,j}}{\partial x_j} = 0 \tag{10}$$

$$\frac{\partial \rho_l \overline{\alpha}_l}{\partial t} + \frac{\partial \rho_l \overline{\alpha}_l \widehat{u}_{l,j}}{\partial x_j} = -\overline{\Gamma} \tag{11}$$

$$\begin{aligned} \frac{\partial \rho_l \overline{\alpha}_l \widehat{u}_{l,i}}{\partial t} + \frac{\partial \rho_l \overline{\alpha}_l \widehat{u}_{l,i} \widehat{u}_{l,j}}{\partial x_j} &= \overline{F}_{d,i} - \widehat{u}_{l,i}\overline{\Gamma} - \frac{\partial \left(-\overline{\tau}^{sgs}_{l,ij}\right)}{\partial x_j} \\ &\quad -\frac{2}{3}\frac{\partial \rho_l \overline{\alpha}_l \widehat{\delta\theta}_l}{\partial x_i} - \frac{\partial \rho_l \overline{\alpha}_l \widehat{\delta R^*}_{l,ij}}{\partial x_j} \end{aligned} \tag{12}$$

$$\frac{\partial \rho_l \overline{\alpha}_l \widehat{h}_l}{\partial t} + \frac{\partial \rho_l \overline{\alpha}_l \widehat{u}_{l,j} \widehat{h}_l}{\partial x_j} = -\widehat{h}_l \overline{\Gamma} + \overline{\Phi}_l \tag{13}$$

$$\frac{\partial \rho_l \overline{\alpha}_l \widehat{\delta\theta}_l}{\partial t} + \frac{\partial \rho_l \overline{\alpha}_l \widehat{u}_{l,j} \widehat{\delta\theta}_l}{\partial x_j} = \overline{P} - \overline{S} \tag{14}$$

where the subgrid diffusion term of liquid enthalpy is neglected. The filtered drag-force contribution is written $\overline{\mathbf{F}}_d$, the filtered evaporation rate is denoted $\overline{\Gamma}$. $\overline{\Phi}_l$ is the filtered ensemble average of the conductive heat flux on the liquid side at the droplet surface ϕ_p^c. Details on the source terms are provided in subsection 2.3. $\overline{\tau}_l^{sgs}$ is the droplet subgrid stress tensor, modeled by analogy to compressible single-phase flows, using a Smagorinsky formulation for the trace-free part together with a Yoshizawa formulation for the trace

part (Moreau et al., 2010):

$$\overline{\tau}^{sgs}_{l,ij} = -\rho_l \overline{\alpha}_l \left(-C_S^2 \Delta^2 \left\| \widehat{S^*_l} \right\| \widehat{S^*_{l,ij}} + C_Y \Delta^2 \left\| \widehat{S^*_l} \right\|^2 \delta_{ij} \right) \quad (15)$$

$$\text{with:} \qquad \widehat{S^*_{l,ij}} = \left(\frac{\partial \widehat{u}_{l,i}}{\partial x_j} + \frac{\partial \widehat{u}_{l,j}}{\partial x_i} \right) - \frac{2}{3} \frac{\partial \widehat{u}_{l,k}}{\partial x_k} \delta_{ij} \quad (16)$$

$$\left\| \widehat{S^*_l} \right\|^2 = \frac{1}{2} \widehat{S^*_{l,ij}} \widehat{S^*_{l,ij}} \quad (17)$$

where the constants are set to $C_S = 0.16$ and $C_Y = 0.051$.

$\widehat{\delta R^*}_l$ is the deviatoric part of the second-order random uncorrelated velocity correlation tensor $\widehat{\delta R}_l$:

$$\overline{\alpha}_l \widehat{\delta R}_{l,ij} = \overline{\left\langle \breve{\alpha}_l u''_{p,i} u''_{p,j} | \mathcal{H}_f \right\rangle_l} = \overline{\alpha}_l \left(\widehat{\delta R^*}_{l,ij} + \frac{2}{3} \widehat{\delta\theta}_l \delta_{ij} \right) \quad (18)$$

It is linked to the strain rate of the mesoscopic motion through a viscosity model (Simonin, 1996; Sakiz and Simonin, 1998; Simonin et al., 2002):

$$\rho_l \overline{\alpha}_l \widehat{\delta R^*}_{l,ij} = 2\,\mu_{rum} \left[\frac{1}{2} \left(\frac{\partial \widehat{u}_{l,j}}{\partial x_i} + \frac{\partial \widehat{u}_{l,i}}{\partial x_j} \right) + \frac{1}{3} \frac{\partial \widehat{u}_{l,k}}{\partial x_k} \delta_{ij} \right] \quad (19)$$

$$\text{with:} \qquad \mu_{rum} = \frac{1}{3} \rho_l \overline{\alpha}_l \tau_p \widehat{\delta\theta}_l \quad (20)$$

In Eq. (14), the terms $\overline{P}$ and $\overline{S}$ refer to the production and sink terms respectively to model transfer of energy between the correlated and uncorrelated motions at the resolved and subgrid scales. It includes second and third-order velocity correlations modeled with gradient laws (Sakiz and Simonin, 1998; Riber, 2007).

In the Euler-Euler approach, the TTGC scheme is also used to solve the set of equations (10)-(14). The dispersed phase behaves as a highly compressible inviscid flow, leading to locally high particle number density (Squires and Eaton, 1991; Kaufmann et al., 2008) and requiring the use of artificial viscosity of 2^{nd} and 4^{th} order in these zones.

In the EL simulations, particle-wall interactions are modeled through elastic rebound. In the EE approach, the implementation of a rebound condition is not straightforward as there is no notion of particle path. In the present simulations, a slip condition is used instead, ensuring wall impermeability.

2.3. Interphase exchange terms

The Lagrangian and Eulerian approaches integrated into the AVBP solver use the same models to account for the drag force and the evaporation process.

2.3.1. Drag force

Considering spherical droplets and high particle to fluid density ratio ($\rho/\rho_l \ll 1$) without gravity effect the drag force can be taken as the Stokes drag force extended by the Schiller and Naumann's correlation (1933).

$$f_{p,i} = -\frac{m_p}{\tau_p}\left(u_{p,i} - \widetilde{u}_{g@p,i}\right) \quad \text{with:} \quad \tau_p = \frac{\rho_l\, d^2}{18\mu}\,\frac{1}{1+0.15Re_p^{0.687}} \tag{21}$$

where $\widetilde{\mathbf{u}}_{g@p}$ is the gaseous velocity *seen* by the droplet.

In the Lagrangian approach, $\widetilde{\mathbf{u}}_{g@p}$ is a linear interpolation from the filtered gas field at the droplet position, without accounting for the subgrid scale contribution. In the Eulerian approach the gaseous velocity *seen* by the dispersed liquid phase is the filtered gas velocity at the same node location, leading to the expression:

$$\overline{F}_{d,i} = \rho_l\overline{\alpha}_l\,\overline{\left\langle \frac{f_{p,i}}{m_p}|\mathcal{H}_f\right\rangle_l} = -\frac{\rho_l\overline{\alpha}_l}{\tau_p}\left(\widehat{u}_{l,i} - \widetilde{u}_i\right) \tag{22}$$

2.3.2. Evaporation source terms

The evaporation model is derived for an isolated spherical droplet at the thermodynamic equilibrium with a surrounding quiescent mixture of ideal gas. Within the assumption of infinitely fast thermal conductivity in the liquid, the evaporating rate $\dot{m}_p$ and the gas conductive flux at the droplet surface ϕ_g^c are (Sirignano, 1999; Kuo, 2005):

$$\dot{m}_p = -\pi d\, Sh\, [\rho D_F] \ln(1 + B_M) \tag{23}$$

$$\phi_g^c = -\pi d\, Nu\, \lambda\, (T_\infty - T_p)\, \frac{\ln(1 + B_T)}{B_T} \tag{24}$$

where B_M and B_T stand for the Spalding numbers of mass and temperature respectively, accounting for the gas mixture modification in the gaseous layer surrounding the droplet, following the $1/3^{rd}$-$2/3^{rd}$ rule (Hubbard et al., 1975). According to the thermodynamic equilibrium hypothesis, the Clausius-Clapeyron equilibrium vapor pressure relationship allows to determine the fuel mass fraction at the droplet surface for the evaluation of B_M. The balance between gas and liquid conductive and convective heat fluxes gives the conductive heat flux on the liquid side:

$$\phi_p^c = -\phi_g^c + \dot{m}_p L_v\, (T_p) \tag{25}$$

where $L_v\, (T_p)$ is the latent heat of vaporization at the droplet temperature. The Nusselt (Nu) and Sherwood (Sh) numbers are modified following Frössling (1938) to account for the effect of non-vanishing slip velocity between droplet and carrier phase.

In the Lagrangian approach, far field values T_∞ and $Y_{k,\infty}$ are linearly interpolated from the gaseous filtered fields at the droplet position. In the

Eulerian approach these values are the gaseous filtered fields at the node. The source terms for the Eulerian approach are :

$$\overline{\Gamma} = \rho_l \overline{\alpha}_l \overline{\left\langle \frac{-\dot{m}_p}{m_p} | \mathcal{H}_f \right\rangle_l} = \pi \overline{n}_l d\, Sh\, [\rho D_F] \ln(1 + B_M) \quad (26)$$

$$\overline{\Phi}_l = \rho_l \overline{\alpha}_l \overline{\left\langle \frac{\phi_p^c}{m_p} | \mathcal{H}_f \right\rangle_l} = \pi \overline{n}_l\, d\, Nu\, \lambda \left(\widetilde{T} - \widehat{T}_l \right) \frac{\ln(1 + B_T)}{B_T} - \overline{\Gamma}\, L_v(\widehat{T}_l) \quad (27)$$

2.3.3. Source terms in the gas phase equations

The source terms $\overline{\dot{s}}_{mo,i}$, $\overline{\dot{s}}_{en}$ and $\overline{\dot{s}}_{ms,k}$ in the gas phase equations (1)-(3) write in the EE formulation:

$$\overline{\dot{s}}_{mo,i} = \overline{\Gamma} \widehat{u}_{l,i} - \overline{F}_{d,i} \quad (28)$$

$$\overline{\dot{s}}_{en} = -\overline{\Phi}_l + \widehat{h}_l \overline{\Gamma} + \overline{\Gamma} \left(\frac{1}{2} \widehat{u}_{l,i}^2 \right) - \widehat{u}_{l,i} \overline{F}_{d,i} \quad (29)$$

$$\overline{\dot{s}}_{ms,k} = \overline{\Gamma} \delta_{kF} \quad (30)$$

In the EL formalism, the gaseous source terms are the volume weighted sum of source terms over the particles located in all grid elements containing the considered node, taking the conservative weight $w_{p@n}$ for a particle p as a function of its distance to the considered node (Saffman, 1973):

$$\overline{\dot{s}}_{mo,i} = -\frac{1}{V} \sum_{p=1}^{N_p} w_{p@n} \left(\dot{m}_p u_{p,i} + f_{p,i} \right) \quad (31)$$

$$\overline{\dot{s}}_{en} = -\frac{1}{V} \sum_{p=1}^{N_p} w_{p@n} \left(\phi_g^c - \dot{m}_p\, h_{s,F}(T_p) + \dot{m}_p \left(\frac{1}{2} {u_{p,i}}^2 \right) + f_{p,i} u_{p,i} \right) \quad (32)$$

$$\overline{\dot{s}}_{ms,k} = -\frac{1}{V} \sum_{p=1}^{N_p} w_{p@n} \left(\dot{m}_p \delta_{kF} \right) \quad (33)$$

3. The FIM-UR methodology

When performing LES of a liquid fueled combustion chamber, the main difficulty lies in the lack of information on spray characteristics at injection.

It is however a crucial information as the spray size and velocity distributions have an important impact on the flame in the chamber. In most cases, the pressure drop or the spray angle at a calibrated flow rate (measured sometimes with an other liquid than the fuel) and the liquid flow rate are the only available parameters. The diameter distribution and the velocity field are sometimes (rarely) measured but only far downstream (about ten to twenty millimeters) in the combustion chamber.

The proposed methodology complements this partial information. It relies on a minimal number of internal geometrical parameters for pressure-swirl atomizer of the *simplex* type, on balance equations applied to the gas-liquid mixture in the vicinity of the discharge orifice and on the knowledge of the mean drop size of the produced spray. The resulting *model* atomizer may then be used to prescribe liquid inflow characteristics.

3.1. The simplex *atomizer*

Pressure-swirl atomizers are very effective as they produce a thin liquid sheet which is quickly destabilized into ligaments which break-up further into small drops. The resulting distribution patterns are delimited within a specific spray angle with the shape of hollow or solid cone.

The internal geometry of a simplex atomizer (Bayvel and Orzechowski, 1993) is illustrated in Fig. 1. The liquid is injected tangentially through a single channel **1** of diameter d_p in the swirl chamber **2** of diameter D_S. The injection surface A_p of the swirl chamber is defined by $A_p = \frac{\pi d_p^2}{4}$. The discharge channel **3** ends up in an orifice of radius R_0. The high rotation velocity creates an air core in the orifice channel (Lefebvre, 1989), of radius R_a at the discharge orifice. The liquid comes out in a hollow cone thin liquid

sheet of half angle θ_S

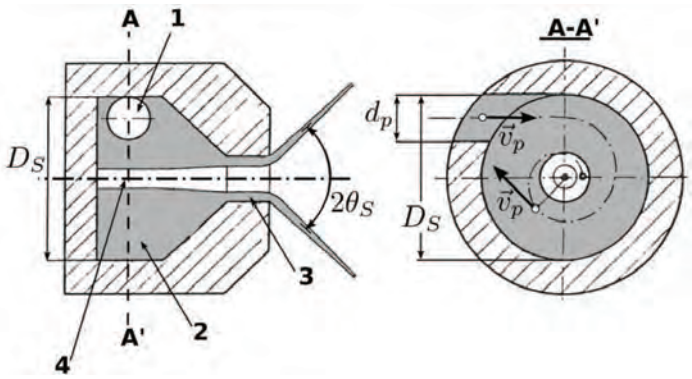

Figure 1: Internal geometry parameters of a simplex atomizer. The grey shaded surfaces represent the liquid path, the hatched surfaces represent the solid body of the atomizer. From (Lefebvre, 1989).

The spray angle depends on the design of the swirl chamber and the discharge orifice (Rizk and Lefebvre, 1985). The spray diameter distribution depends on the thickness of the film (Rizk and Lefebvre, 1980) and the liquid velocity. It also depends on the liquid properties (Rizk and Lefebvre, 1983) of the injected fuel, such as density, viscosity and surface tension. The atomization process is also highly dependent on the characteristics of the surrounding air stream (Dombrowski and Johns, 1963), such as pressure and relative velocity to the liquid. Finally turbulence plays also a role, as it may amplify the surface waves, reducing the breakup distance and influencing the mean drop size (Fraser et al., 1963).

The half-spray angle can be exclusively estimated from geometric parameters and calibration values. For the mean diameter of the droplet distribution, many empirical correlations exist but they have no general character.

As a consequence, the present monodisperse model relies on measurements for the mean diameter.

The empirical formula of Rizk and Lefebvre (1985) correlates the half-spray angle θ_S to the ratio X of the air core surface A_{air} and the discharge orifice surface A_{exit}:

$$X = \frac{A_{air}}{A_{exit}} = \left(\frac{R_a}{R_0}\right)^2 = \frac{\sin^2\theta_S}{1+\cos^2\theta_S} \tag{34}$$

From the inviscid theory, the discharge coefficient C_D can be related to the contraction factor of the orifice X (Lefebvre, 1989):

$$C_D = 1.17\sqrt{\frac{(1-X)^3}{(1+X)}} \tag{35}$$

The adapted formula of Taylor (1948) (Lefebvre, 1989) is used to estimate the tangential-injection surface A_p:

$$A_p = 20.73\, C_D^2\, A_0 \tag{36}$$

where $A_0 = \pi\, R_0^2$ is the total discharge orifice surface.

If the spray angle is unknown, the discharge coefficient of the real injector is determined directly from the injection pressure at a calibration flow rate $\dot{m}_l^c$ as:

$$C_D = \frac{\dot{m}_l^c}{A_0\sqrt{2\,\rho_l \Delta P_i}} \tag{37}$$

Then A_p is estimated with Eq. (36), and θ_S is estimated from Eqs. (34) and (35).

3.2. FIM-UR principles

A sketch of the FIM-UR methodology is shown in Fig. 2. The spray formed at the exit of the atomizer is supposed to be axisymmetric around the

(Ox) axis. Cylindrical coordinates (r, θ, x) are used. The discharge orifice is placed at $x = x_0$, referred as the *real* injection plane. The half spray angle θ_S is defined in a meridian plane as the angle between the main spray direction (Ox') and the symmetry axis (Ox). The radial position along the main spray direction at the abscissa x is written $R_S(x) = R_S^0 + (x - x_0)\tan\theta_S$ where R_S^0 is the radial position of the center of the cylindrical liquid film at $x = x_0$.

In the EL approach, liquid droplets of diameter d are injected over a ring of outer radius R_0 (the radius of the discharge orifice) and inner radius R_a (the radius of the air core at $x = x_0$), with a velocity $\mathbf{u}_l^0$.

In the EE formalism, the strategy is to place the fuel injection downstream of the *real* injection plane to avoid meshing the very narrow surface of the discharge orifice (less than 1 mm diameter), which would lead to too high computational expense. As the spray opens, the radius R_i of the injection surface at the shifted plane $(x = x_i)$ increases. In the EE approach, liquid is injected through the disk $\{x = x_i, r \in [0, R_i]\}$, where the liquid volume fraction α_l^i, the droplet diameter d and the liquid velocity $\mathbf{u}_l^i$ profiles are prescribed. Due to air entrainment between x_0 and x_i, gas inflow conditions must also be determined. All quantities in the $x = x_i$ plane are derived from their values at $x = x_0$ through balance equations.

The FIM-UR methodology may be summarized as follows:

1. First, unknown design parameters of the atomizer are determined and the boundary conditions on the *real* injection plane $x = x_0$ are derived. This defines the injection boundary conditions for the EL approach.
2. Second, integral conservation laws for the spray between the planes $x = x_0$ and $x = x_i$ are written, using the values at the *real* injection

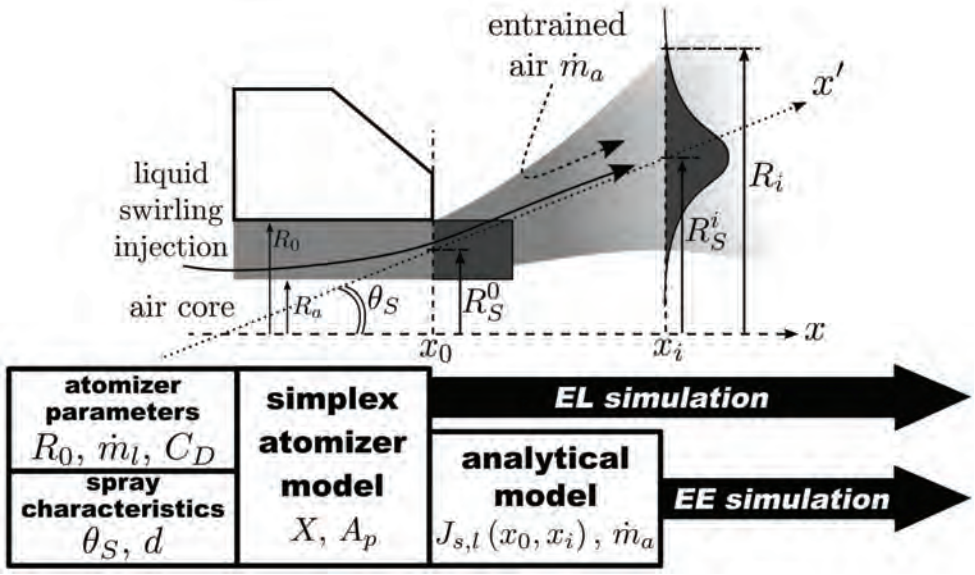

Figure 2: Definition of parameters and sketch of the FIM-UR methodology.

plane derived in the previous step.

3. Third, the air mass flow rate entrained by the spray $\dot{m}_a$ and the momentum loss $J_{s,l}$ between $x = x_0$ and $x = x_i$ must be calculated to close the derived balance equations. Their derivation following the Cossali's model (Cossali, 2001) is given in Appendix A. This allows to determine all boundary conditions for gas and liquid at $x = x_i$ in the EE approach.

These three steps are detailed below.

3.3. Modeling the injection boundary conditions

Step 1: Injection profiles in the discharge orifice plane $x = x_0$

The liquid velocity and volume fraction profiles on the discharge orifice

$(x = x_0)$ are given by:

$$u^0_{l,r}(\theta, r_0) = 0 \tag{38}$$

$$u^0_{l,\theta}(\theta, r_0) = \frac{\dot{m}_l}{\rho_l A_p} \frac{r_0}{R^0_S} \tag{39}$$

$$u^0_{l,x}(\theta, r_0) = \frac{\dot{m}_l}{\rho_l \pi R_0^2 (1 - X)} \tag{40}$$

$$\alpha^0_l(\theta, r_0) = \begin{cases} 0 & \text{if } r_0 \in [0, R_a] \\ 1 & \text{if } r_0 \in [R_a, R_0] \end{cases} \tag{41}$$

where R^0_S stands for the middle position of the liquid sheet: $R^0_S = \frac{R_0 + R_a}{2}$. The spray opening is represented by the linear radial dependence of the tangential velocity and the volume fraction is set to zero in the air core.

Step 2: Spray evolution from $x = x_0$ to $x = x_i$

From the real $(x = x_0)$ to the simulated $(x = x_i)$ injection plane, integral balances of mass and momentum are derived. The momentum exchange between the liquid and the gas phases is restricted to the drag force, responsible for air entrainment by the spray. Evaporation is not taken into account and the droplet diameter d remains constant.

For the liquid phase in the shifted injection plane $(x = x_i)$, further assumptions are used to simplify the determination of the droplet velocity and volume fraction distributions:

1. The liquid spray keeps its axisymmetrical shape around the (Ox) axis.
2. The droplet-axial velocity does not depend on the radial coordinate.
3. A Gaussian profile is assumed for the liquid volume fraction.

Expressions of the liquid volume fraction and velocity components in the injection plane $x = x_i$ take then the form :

$$u^i_{l,r}(\theta, r) = u^i_{l,r}(r) \quad (42)$$

$$u^i_{l,\theta}(\theta, r) = u^i_{l,\theta}(r) \quad (43)$$

$$u^i_{l,x}(\theta, r) = u^i_{l,x}|_{mean} \quad (44)$$

$$\alpha^i_l(\theta, r) = \alpha^i_l|_{max} \cdot e^{\frac{-(r-\mu)^2}{\sigma^2}} \quad (45)$$

This formulation introduces 4 parameters ($u^i_{l,x}|_{mean}$, $\alpha^i_l|_{max}$, μ and σ) and 2 functions ($u^i_{l,r}(r)$ and $u^i_{l,\theta}(r)$), determined by applying conservation equations between $x = x_0$ and $x = x_i$.

Mass conservation

The liquid mass flow rate through the disk $x = x_i, r \in [0, R_i]$ is equal to the total injected liquid mass flow rate $\dot{m}_l$:

$$\dot{m}_l = \int_0^{R_i} \int_0^{2\pi} \rho_l u^i_{l,x} \alpha^i_l r d\theta dr \quad (46)$$

Assuming a constant spray angle (Fig. 2), the Gaussian volume fraction distribution is centered on $\mu = R_S(x_i) = R^0_S + (x_i - x_0)\tan\theta_S \equiv R^i_S$. Using Eqs. (44) and (45), the previous equation can be integrated analytically, yielding:

$$\dot{m}_l = \pi \rho_l u^i_{l,x}|_{mean}\, \alpha^i_l|_{max} \left[\sigma^2 \left(1 - \exp\left(\frac{-{R_i}^2}{\sigma^2}\right)\right) + \sigma R^i_S \sqrt{\pi}\, \mathrm{erf}\left(\frac{R_i}{\sigma}\right)\right] \quad (47)$$

$$= \pi \rho_l u^i_{l,x}|_{mean}\, \alpha^i_l|_{max} I_\alpha \quad (48)$$

The width of the Gaussian profile of the liquid volume fraction is determined so that the spray edges correspond to a volume fraction of 2% of its maximum value: $\alpha^i_l(R_i) = 0.02\, \alpha^i_l|_{max}$. This gives $\sigma^2 = -(R_i - R^i_S)^2 \,/\, \ln 0.02$.

Axial momentum conservation

The balance of momentum writes:

$$J_{l,x}^{i} = J_{l,x}^{0} + J_{s,l}\left(x_0, x_i\right) \tag{49}$$

where $J_{l,x}^{0}$ and $J_{l,x}^{i}$ are the axial liquid momentum flux at respectively $x = x_0$ and $x = x_i$ and $J_{s,l}\left(x_0, x_i\right)$ is the momentum exchange due to drag. The fluxes $J_{l,x}^{0}$ and $J_{l,x}^{i}$ can be calculated by integration of the momentum flux over the discharge orifice plane and the translated injection plane respectively:

$$J_{l,x}^{0} = \int_0^{R_0} 2\pi\rho_l\alpha_l^0\left(u_{l,x}^{0}\right)^2 r dr = \dot{m}_l\, u_{l,x}^{0} \tag{50}$$

$$J_{l,x}^{i} = \int_0^{R_i} 2\pi\rho_l\alpha_l^i\left(u_{l,x}^{i}\right)^2 r dr = \dot{m}_l\, u_{l,x}^{i}|_{mean} \tag{51}$$

The momentum sink $J_{s,l}\left(x_0, x_i\right)$ is calculated in Appendix A.3, by applying the integral model developed by Cossali (2001).

Combining Eqs. (40), (50) and (51), the liquid axial velocity is obtained:

$$u_{l,x}^{i}|_{mean} = u_{l,x}^{0} + \frac{J_{s,l}\left(x_0, x_i\right)}{\dot{m}_l} \tag{52}$$

Angular momentum conservation

The momentum exchange between the injected liquid and the ambient fluid (air) is supposed most prominent in the (Ox) injection direction and is neglected in the perpendicular directions. As a consequence, the droplet trajectory projected in a plane perpendicular to the (Ox) injection direction follows a ballistic trajectory: a droplet initially located at a radial position $r_0 \in [0, R_0]$ in the plane $x = x_0$ follows a straight line when projected perpendicular to the injection axis (Fig. 3).

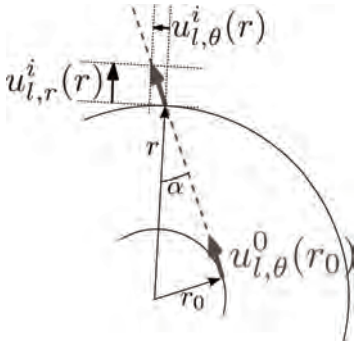

Figure 3: Projection of the ballistic trajectory of the droplet in the plane normal to the injection direction x.

On the plane $x = x_i$ the droplet is located at the radial distance $r \in [0, R_i]$. As the radial velocity is null at $x = x_0$, the radial and azimuthal velocity components in the injection plane $x = x_i$ are given by:

$$u^i_{l,r}(r) = u^0_{l,\theta}(r_0)\cos\alpha = u^0_{l,\theta}(r_0)\frac{\sqrt{r^2 - r_0^2}}{r} \tag{53}$$

$$u^i_{l,\theta}(r) = u^0_{l,\theta}(r_0)\sin\alpha = u^0_{l,\theta}(r_0)\frac{r_0}{r} \tag{54}$$

where the angle α is defined in Fig. 3 as the angle between the projected droplet position vectors. Eq. (54) can be seen as the conservation of the angular momentum of the droplets around the x-rotational axis.

If the distance between the real and the simulated injection plane is small enough, the constant spray angle ensures that r_0 and r are related by:

$$\frac{r}{r_0} \simeq \frac{R^i_S}{R^0_S} \tag{55}$$

Combining Eqs. (39) and (53)-(55), the liquid radial and azimuthal velocities on the injection plane are finally related to the discharge orifice pa-

rameters:

$$u_{l,r}^{i}(r) = \frac{\dot{m}_l}{\rho_l A_p}\sqrt{1-\left(\frac{R_S^0}{R_S^i}\right)^2}\,\frac{r}{R_S^i} \quad (56)$$

$$u_{l,\theta}^{i}(r) = \frac{\dot{m}_l}{\rho_l A_p}\,\frac{R_S^0}{R_S^i}\,\frac{r}{R_S^i} \quad (57)$$

Step 3: Air entrainment by the spray from $x = x_0$ to $x = x_i$

As air is entrained by the spray, gas boundary conditions are also required in the plane $x = x_i$. Experimental results by Prosperi et al. (2007) demonstrated that the air flow rate entrained by the spray scales like the distance to the atomizer-discharge orifice to the power 3/2 and like the gas density to the power 5/6 in the near field of a hollow-cone spray. These results confirm the validity of the integral model obtained by Cossali (2001) in the near-field of the atomizer which states that the air entrained by the spray is proportional to $\rho^{5/6}(x-x_0)^{3/2}$. It is assumed that the axial velocity for the gas phase is independent of the radial coordinate: $u_{g,x}(x,r) = u_{g,x}(x)$.

The mass-flow rate of the air entrained by the spray at the axial position x_i can therefore be expressed as $\dot{m}_a = \pi {R_i}^2 \rho u_{g,x}^i$, where $u_{g,x}^i = u_{g,x}(x_i)$, and according to Prosperi et al. (2007):

$$\dot{m}_a = K_a\,\rho^{5/6}(x_i - x_0)^{3/2} \quad (58)$$

Combining the two above expressions for $\dot{m}_a$, the gas axial velocity is finally found to be:

$$u_{g,x}^i = \frac{K_a\,(x_i - x_0)^{3/2}}{\pi {R_i}^2 (\rho)^{1/6}} \quad (59)$$

At this stage, the missing parameters are the outer radius of the spray R_i, the coefficient for air entrained by the spray K_a, which is a constant

for a given atomizer (Prosperi et al., 2007), and the momentum exchange $J_{s,l}(x_0, x_i)$. Appendix A describes a way to determine these parameters, by applying the integral model developed by Cossali (2001).

Introducing the parameter A_u, Eq. A.21, which takes into account contraction effects on the discharge orifice as well as air entrainement effects along the axial distance, the liquid velocity profiles on the simulated injection plane $x = x_i$ are finally written:

$$u^i_{l,r}(\theta, r) = \frac{\dot{m}_l}{\rho_l A_p}\sqrt{1 - \left(\frac{R^0_S}{R^i_S}\right)^2}\,\frac{r}{R^i_S} \tag{60}$$

$$u^i_{l,\theta}(\theta, r) = \frac{\dot{m}_l}{\rho_l A_p}\frac{R^0_S}{R^i_S}\frac{r}{R^i_S} \tag{61}$$

$$u^i_{l,x}(\theta, r) = \frac{\dot{m}_l}{\pi R^2_0}\,A_u \tag{62}$$

$$\alpha^i_l(\theta, r) = \frac{\pi R^2_0}{\rho_l\, I_\alpha\, A_u}\, e^{\frac{-(r-\mu)^2}{\sigma^2}} \tag{63}$$

Such a methodology has been developed here in the context of mono-disperse spray and be easily extended for poly-disperse sprays (Vié et al., 2010).

4. Application to the MERCATO configuration

4.1. Experimental setup

Two-phase flow LES simulations including the injection boundary profiles defined within the FIM-UR methodology are performed on the MERCATO test-rig. This work was first initiated by Lamarque (2007). The experimental rig MERCATO (Fig. 4) is a swirled combustor fed with air and liquid kerosene (Jet-A) operated at ONERA-Fauga by R. Lecourt and coworkers (García-Rosa, 2008). For easy optical access, the plenum and combustion chamber

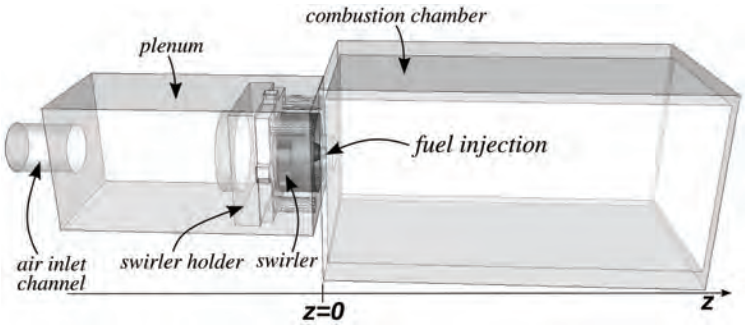

Figure 4: The MERCATO configuration (ONERA Fauga)

have square sections of respectively 100 mm and 130 mm side length. They are respectively 200 mm and 285 mm long. The air goes from the plenum to the combustion chamber through the twelve tilted channels of a single staged swirler and discharges into the diffuser, a long cylindrical channel which ends up into the combustion chamber. The liquid kerosene is injected through a pressure-swirled atomizer located on the tip of the nozzle of the air injection system. Characteristic parameters of the *Delavan* atomizer (Tab. 1) have been determined by calibration.

Discharge orifice	$R_0 = 0.25 \quad \text{mm}$
Half-spray angle	$\theta_s = 40^\circ$
Injection pressure at calibration	$\Delta P_i^c = 6.89 \times 10^5 \quad \text{Pa}$
Liquid flow-rate for calibration	$\dot{m}_l^c = 3.3 \quad \text{g/s}$

Table 1: Characteristic parameters of the atomizer.

The flow regimes considered in this paper are presented in Table 2. Case I is a purely gaseous flow while Case II is a two-phase evaporating flow. The

air is heated up to 463 K to enhance evaporation and reduce the formation of liquid fuel films on visualization windows during experiments.

Case	Pressure	Temp. (K)		Flow rate (g/s)	
	(atm)	Liquid	Air	Air	Fuel
I: gas flow	1	–	463	15	–
II: gas flow + droplets	1	300	463	15	1

Table 2: Summary of operating points for the two simulated cases.

For Case I, LDA (laser doppler anemometry) measurements were performed on the gas seeded with fine oil droplets ($< 2\mu$m). The mean and root-mean-square (RMS) of the three gas velocity components were obtained in five transverse planes ($z = 6$ mm, $z = 26$ mm, $z = 56$ mm, $z =$86 mm, $z = 116$ mm), z being the axial distance from the inlet plane of the combustion chamber. For Case II, LDA-PDA (phase doppler anemometry) measurements were performed on the kerosene dispersed phase to obtain the mean and RMS of the three velocity components and the diameter of the droplets in three transverse planes ($z = 6$ mm, $z = 26$ mm, $z = 56$ mm). Case I measurements allow to validate the gas phase solver, while Case II data allows to evaluate the dynamics of the dispersed phase and the dispersion of droplet sizes into the combustion chamber in both Eulerian and Lagrangian approaches. Data over the first measurement plane at $z = 6$ mm will be used to evaluate the validity of the FIM-UR methodology for a complex flow.

The MERCATO geometry is fully meshed with tetrahedral cells in order to efficiently refine or coarsen cells in areas of interest (swirler, combustion chamber) or non-interest (plenum, atmosphere outlet) respectively. A grid

convergence study has led to the grid shown in Fig. 5, which contains 650000 nodes mesh (3.5 million tetrahedral cells).

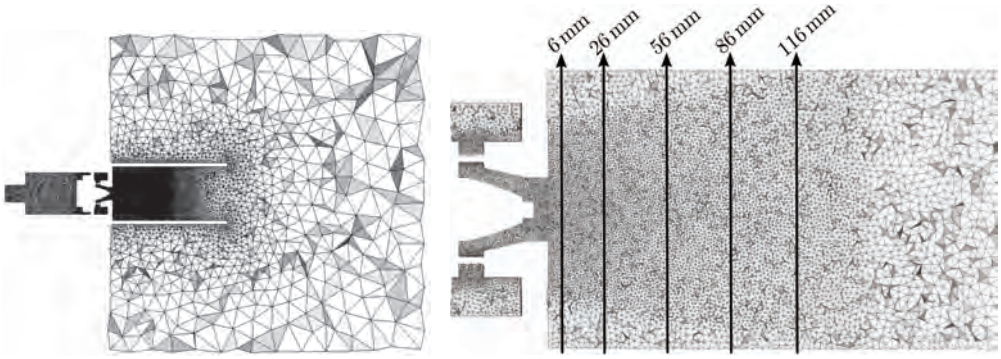

(a) Global view of the configuration, from inlet to atmospheric outlet.

(b) Detailed view in the measurement area.

Figure 5: Mid-section plane of the unstructured mesh for the present simulations.

4.2. Liquid injection

Jet-A kerosene is a fuel used for civil aviation. It is a complex mixture of hundreds of hydrocarbons and additives and is usually represented by surrogate fuels, composed of few hydrocarbons (Dagaut and Cathonnet, 2006). In the present simulations Jet-A kerosene is modeled by a single *meta* species, called KERO_LUCHE, built as an average of the gaseous thermodynamic properties of the 3 components surrogate of Luche (2003) (74% of n-decane, 15% propyl-benzene, 11% propyl-cyclo-hexane per unit volume). The liquid properties are computed from the correlation functions proposed by Harstad and Bellan (2004) for Jet-A, using the mean molar weight of the surrogate, $W_F = 137.2$ g/mol, as an input parameter. Table 3 summarizes the computed values at 300 K and 1 atm..

Liquid density	781 kg/m^3
Boiling Temperature @ 1atm	445.10 K
Heat of Vaporization	289.01 kJ/kg
Liquid heat capacity	2.003 kJ/kg/K

Table 3: Summary of liquid properties for the *meta*-species KERO_LUCHE.

The FIM-UR methodology is applied to define the inlet conditions for the dispersed phase at the exit of the atomizer. Lagrangian droplets are randomly injected on the nozzle ring $r_0 \in [R_a, R_0]$, and fulfill the velocity-component expressions given in Eqs. (38) - (40). The required parameters for the FIM-UR model at $x = x_0$ have been determined from the calibration parameters (Tab. 1):

Contraction factor	$X = 0.260$
Air core radius	$R_a = 6.5 \times 10^{-5}$ mm
Tangential injection surface	$A_p = 3.5 \times 10^{-7}$ m^2

Table 4: Parameters for the FIM-UR profiles at $x = x_0$.

In the EE formulation the liquid gas mixture is injected on the enlarged nozzle shown in Fig. 6, leading to a translation distance of 2.32 mm and an incircle of radius $R_i = 4$ mm. Table 5 sums up the required parameters for the FIM-UR model evaluated from experimental data given in Tab. 1. The spray is diluted by the entrained air, leading to a liquid volume fraction maximum of $\alpha_l^i|_{max} = 6.51 \times 10^{-3}$ and an axial velocity of $u_{l,x}^i|_{mean} = 8.82$ m/s at injection.

In both the EL and EE simulations, the droplet diameter of the injected

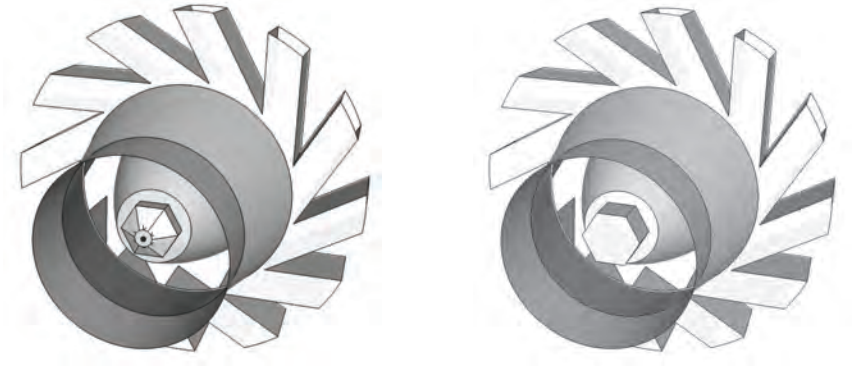

(a) Real nozzle geometry for the EL approach.

(b) Modified nozzle geometry for the EE approach.

Figure 6: Translation of the injection boundary condition.

Spray main radial position	$R_S^i = 2.13$ mm
Liquid volume fraction shape parameter	$\sigma = 8.9 \times 10^{-7}$ m^2
Air entrainment constant	$K_a = 5.62 \times 10^{-4}$
Integration constant	$I_\alpha = 7.10 \times 10^{-6}$
Entrainement parameter	$A_u = 5.44 \times 10^{-3}$

Table 5: Parameters for the FIM-UR profiles at $x = x_i$.

spray is equal to $d = 55$ μm in accordance with the mean diameter of the particle distributions measured by PDA at the first measurement plane. EL injection is monodisperse to lead to comparable results with the EE simulation for which equations and injection model are developed for a mono-disperse spray.

4.3. Characteristic time scales

The behavior of particles in a turbulent flow can be classified into different regimes (Elghobashi, 1994; Balachandar, 2009) depending on their inertial response to the local turbulence characterized by the carrier flow time scale τ_L and the Kolmogorov time scale τ_K and length scale η_K. For the considered operating point, the particle time scale[1] τ_p is 5 ms for a droplet of 55 μm and 0.6 ms for a droplet of 10 μm. Based on the radius of the combustion chamber inlet L=15 mm and a turbulent speed u'=4 m/s (see § 5.1) the following turbulent characteristics can be estimated: τ_L=4 ms, τ_K=0.09 ms, η_K=55 μm and an acceleration $a_K=\eta_K/\tau_K^2$=7000 m/s^2. As $\tau_p \simeq \tau_L$ the droplets dynamics will be highly influenced by the large scale turbulence of the carrier phase and the back coupling of the droplets will significantly disturb the gas flow. For the whole range of particle diameter $\tau_p \gg \tau_K$ ensuring that the subgrid scale turbulence will not have much effects on the droplet dynamics. Moreover the Kolmogorov acceleration is very large compared to the gravity acceleration, so gravity force can be safely ignored.

5. Results

The purely gaseous flow field is validated in a first step and is followed by the two-phase flow simulation results.

[1] without accounting for the Schiller and Naumann (1933) correction, as the slip velocity is unknown at this point.

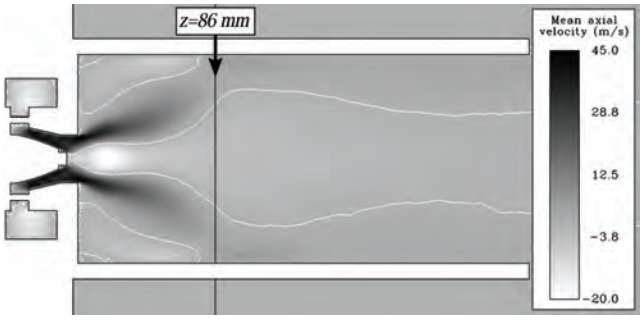

(a) Mean axial velocity field in the mid-section plane. Recirculation zones are highlighted by white contours of null axial velocity.

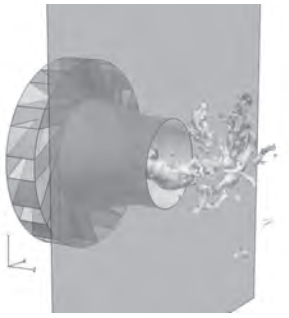

(b) Visualization of the Precessing Vortex Core by an iso-surface of Q-criterion ($Q \approx 2 \times 10^8$ 1/s^2).

Figure 7: Topology of the gas flow in the Mercato test-rig.

5.1. Gas flow without droplets (Case I)

The gaseous flow field of the MERCATO configuration is typical of swirl-stabilized combustors. Due to the sudden expansion of the swirled flow at the combustion chamber inlet, a region of reverse axial flow forms on the axis, called the central toroidal recirculation zone (CTRZ). A precessing vortex core (PVC) (Lucca-Negro and O'Doherty, 2001), spinning at the boundary of the CTRZ at a frequency of 830 Hz is observed in the simulation and detected around the same frequency (778 Hz) in the experimental pressure record. An instantaneous view of the PVC is presented in Fig. 7(b).

In the corners of the combustion chamber, additional zones of reverse axial flow form due to entrainment of air through the gaseous jet, amd are called corner recirculation zones (CRZ). As the jet is strongly confined between these two recirculation zones, a region of high shear is observed in between. The global topology of the gas flow can be deduced from the axial mean

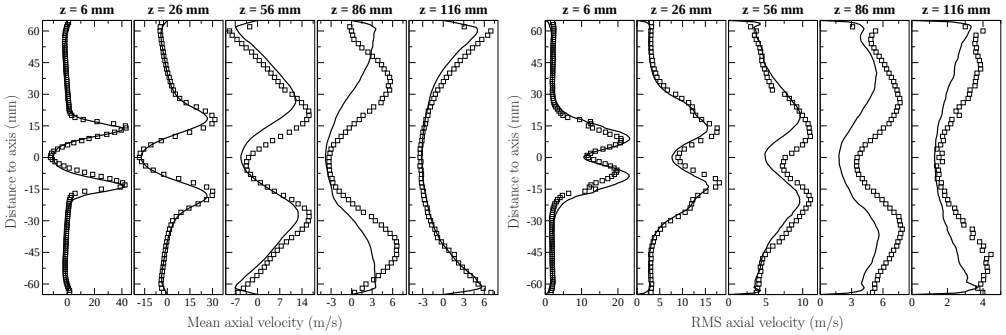

Figure 8: Gaseous axial velocity (Case I). Left: mean, right: RMS. □ LDA, − AVBP

velocity in the mid-section plane of the combustion chamber in Fig. 7(a). Two different regions can be distinguished. First at the inlet of the combustion chamber, the central toroidal recirculation zone is very narrow, confined by the high jet velocities. After the impingement of the swirled jet on the chamber walls, the CTRZ expands suddenly on almost the whole width of the combustion chamber.

Figures 8-10 show mean and RMS gas velocity profiles in the axial, radial and tangential directions respectively for the five axial positions measured from the inlet plane of the combustion chamber. Numerical results (solid lines) are compared with the experimental LDA data (symbols). The averaging time for the purely gaseous simulation is in the order of 780 ms, corresponding to approximately 30 flow-through times. This long simulation time is required to reach a statistic converged state in the recirculation zones (that is symmetric and smooth profile on both mean and RMS components), especially in the last axial position.

Results are in very good agreement with experiments. The LES gas solver is able to accurately reproduce the recirculating flow as well as the high shear

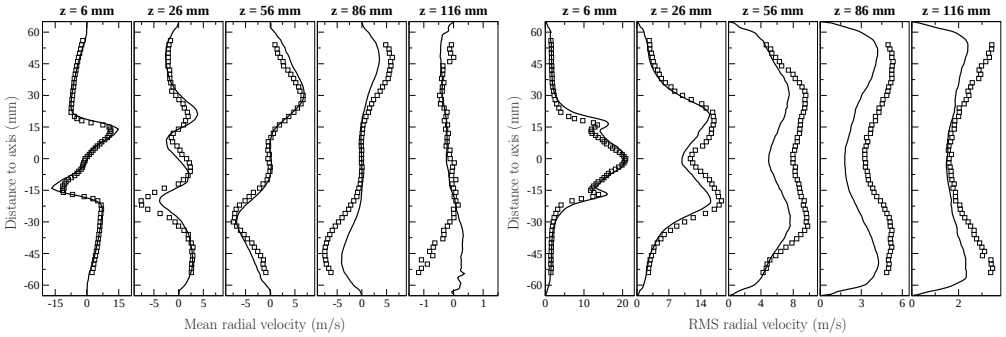

Figure 9: Gaseous radial velocity (Case I). Left: mean, right: RMS. □ LDA, – AVBP

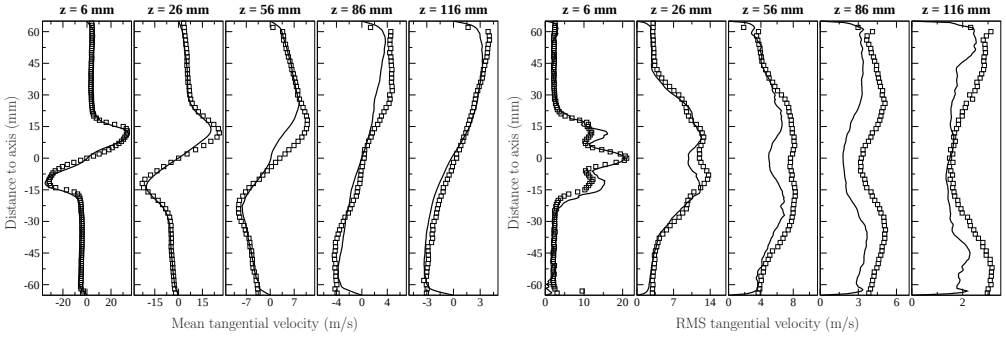

Figure 10: Gaseous tangential velocity (Case I). Left: mean, right: RMS. □ LDA, – AVBP

flow. The radial positions of the maxima for the three components are in fair-good agreement with the experiments ensuring that the opening of the gaseous jet is globally well reproduced, except at the fourth measurement station in Fig. 8 (left) where the opening appears overestimated. RMS velocity profiles are also in excellent agreement with experiment, although underestimated in the most downstream stations due to grid coarsening. It can be noticed in Fig. 7(a) that the measurement plane at $z = 86$ mm is exactly located at the sudden expansion of the CTRZ, which may explain the discrepancies between numerical and experimental profiles of mean and RMS velocity components at this location. Note also the asymmetry of the experimental mean radial profiles (Fig. 9, left), not observed in the numerical simulation. This asymmetry is probably caused by a slight mismatch between the swirler aerodynamic axis and the geometrical axis of the combustion chamber in the experimental setup.

Finally it has been checked that the geometrical modification (Fig. 6) required by the EE FIM-UR boundary condition leads to identical results, even at the first axial location.

5.2. Gas flow with evaporating droplets (Case II)

For case II, droplets are injected starting from a well-established gas-phase solution, following the FIM-UR methodology presented in Section 3.3, with the parameters provided in Section 4.2. The combustion chamber is continuously filled up with droplets which are trapped in the recirculation zones before evaporating entirely.

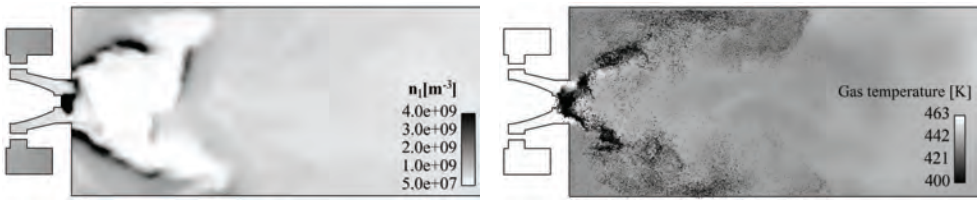

(a) *AVBP-EE: droplet density (grayscale)* (b) *AVBP-EL: droplet positions (dots), gas temperature (grayscale).*

Figure 11: Instantaneous droplet distribution in the Mercato chamber (Case II). Comparison between EE (left) and EL (right)

5.2.1. Liquid phase distribution

Figure 11 shows an instantaneous view of the droplet distribution in the combustion chamber for the EE (Fig. 11(a)) and EL (Fig. 11(b)) simulations. Both capture droplet preferential concentration: the central toroidal recirculation zone has a low droplet density, while dense pockets can be seen in the shear layer of the swirled air jet and droplets are trapped in the corner recirculation zones of the chamber.

These phenomena are further illustrated in Fig. 12, which displays selected particle trajectories extracted from the EL simulation. All trajectories start at the same time and end after complete evaporation of the droplet. All particles follow the strong swirling motion of the air jet, and most of them are trapped in the shear layer of the gaseous jet and rebound against the sidewalls of the combustion chamber at approximately 105 mm. Having lost most of their mass at that time, they closely follow the gaseous flowfield and either remain in the low velocity zone in the vicinity of the sidewalls or are captured in the central toroidal recirculation zone where they rapidly and completely evaporate. Some particles immediately penetrate into the axial

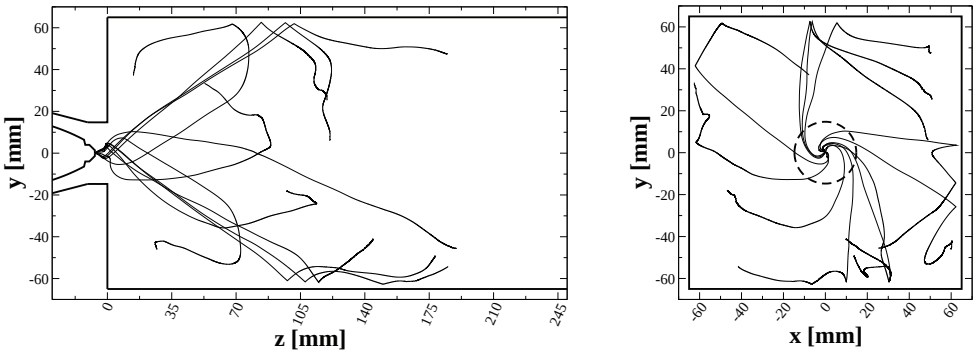

Figure 12: Visualisation of typical particle trajectories in the Lagrangian simulation. Left: side view; right: front view.

recirculation zone where they are strongly deflected. In turn, these particles reverse their axial velocity and are finally captured in the corner recirculation zones of the chamber.

For comparison purposes, particle trajectories may be reconstructed from the EE simulation. Assuming isotropy of the random uncorrelated velocity, and neglecting the unresolved part of the mesoscopic velocity, the particle velocity is locally evaluated by :

$$\mathbf{u}_p^{(k)} = \widehat{\mathbf{u}}_l + \sqrt{2\,\widehat{\delta\theta}_l}\,\mathbf{n}_r(k) \tag{64}$$

where $\mathbf{n}_r(k)$ is a random unity vector. The trajectories along 12 ms of physical time for 8 particles shot simultaneously on the injection boundary patch are presented in Fig. 13. Same particle behaviors as in Fig. 12 are found except near the walls where the slip boundary condition of the EE formulation keeps particles stuck on the walls.

Close to the nozzle, particles are strongly influenced by the PVC, leading to an unsteady tridimensional structure of the dispersed phase shown in Fig. 14. This was also observed during the experimental campaigns: the

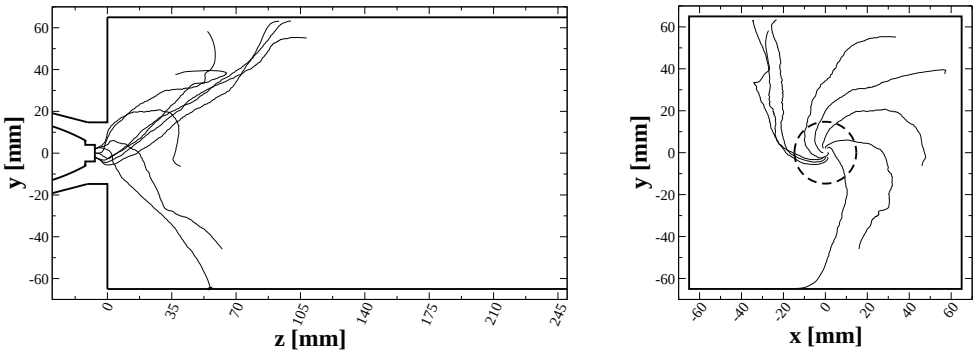

Figure 13: Visualisation of reconstructed particle trajectories in the Eulerian simulation. Left: side view; right: front view.

spray was found unstable and periodically impinged on the walls of the diffuser.

5.2.2. Dynamics of droplet phase

The droplet velocity profiles at three axial planes are compared in Figs. 15 - 17. The averaging time in the two simulations is of the order of 200 ms, corresponding to approximately 5 flow-through times. Note that the air flow rate was increased when performing the droplet LDA measurements at $z = 56$ mm to delay spray impingement on measurement windows. Thus, the comparisons between the LES and the experimental results are affected by larger uncertainties at this location .

Numerical results (lines) presented in Figs. 15 -17 are overall in good agreement with the experimental LDA data (symbols) for both mean and RMS values, and differencies between the Lagrangian (solid line) and Eulerian (dash line) profiles are minor. The EL simulation underestimates the mean axial velocity close to the axis at the first measurement location, which is probably related to the injection procedure as discussed later, and surpris-

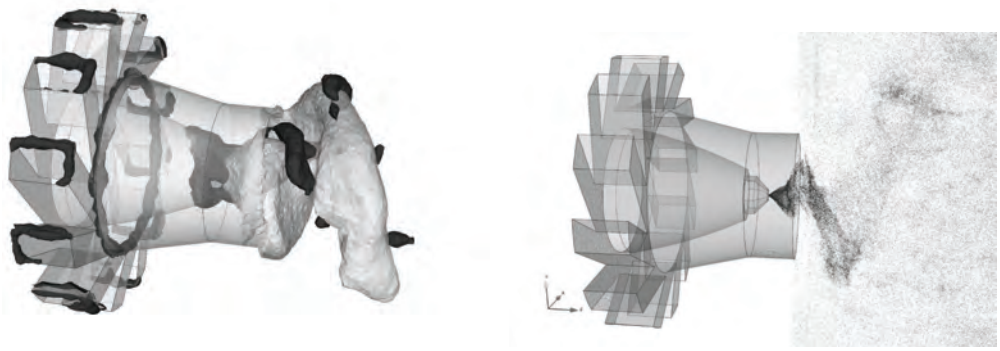

(a) Iso-surface (white) of liquid volume fraction $\overline{\alpha}_l = 5 \times 10^{-5}$ and iso-surface (black) of Q-criterion $Q = 1.2 \times 10^8$ s^2.

(b) Black points mark the droplet position.

Figure 14: Isometric view of the spray close to the injector. Left: EE simulation, right: EL simulation.

ingly overestimates the radial mean velocity maxima at $z = 26$ mm. This EL misprediction of the radial opening of the liquid jet, while EE captures it correctly, is not yet understood. Concerning the mean tangential component (Fig. 16, left) the two simulations only fail in the $z = 56$ mm where the maximum value and slope of tangential velocity are not well predicted.

RMS predictions are overall good in shape and level, and comparable for both approaches. They are less accurate in the last measurement plane, with a better performance of the EL simulation. This is due to the higher diffusivity of the EE approach, resulting in flatter profiles. On the first measurement plane the RMS radial velocity given by the EL simulation highly overpredicts the side peaks, which is again due to the injection boundary condition. Note the oscillations around the center-line of the Lagrangian RMS profiles, due to the poor particle density in this region.

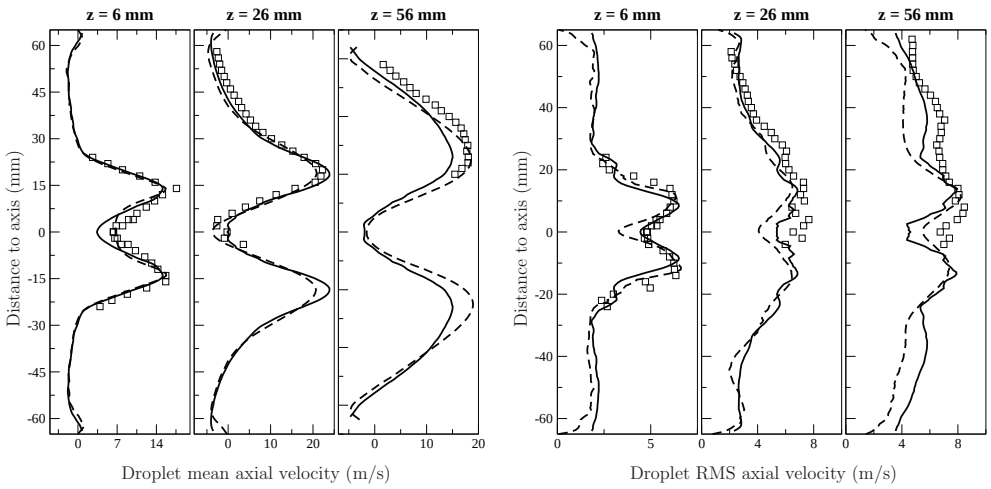

Figure 15: Droplet axial velocity (Case II). Left: mean, right: RMS. □ PDA, – EL, - - EE

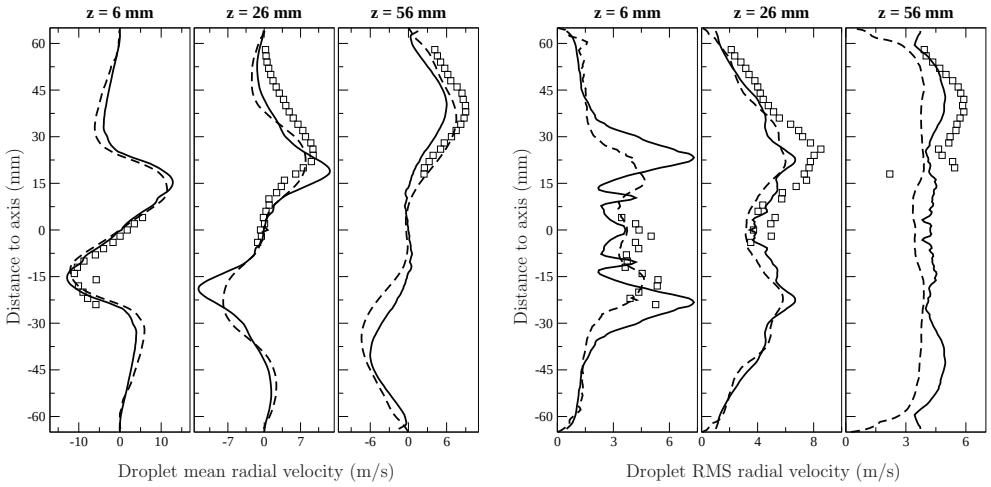

Figure 16: Droplet radial velocity (Case II). Left: mean, right: RMS. □ PDA, – EL, - - EE

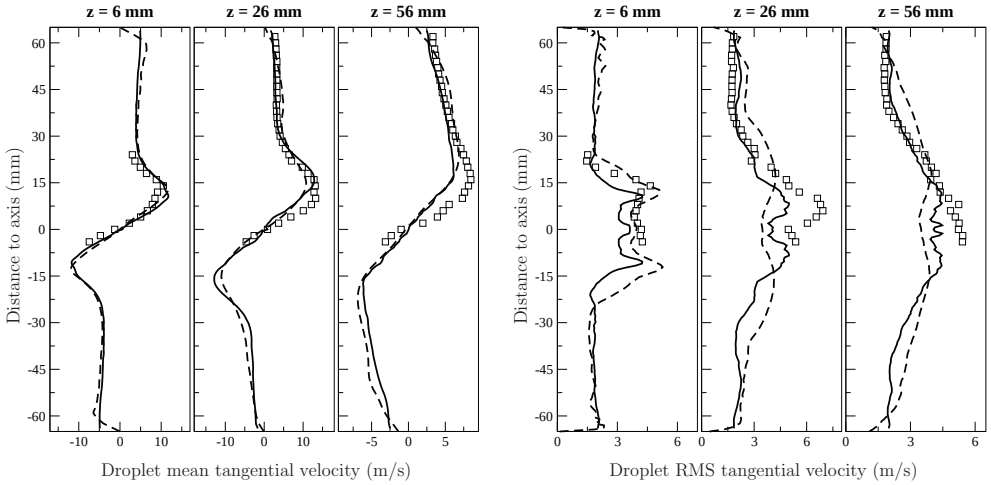

Figure 17: Droplet tangential velocity (Case II). Left: mean, right: RMS. □ PDA, − EL, - - EE

Focusing now on the first profiles at $z = 6$ mm, the results can be related to the FIM-UR injection method. The excellent agreement of the mean and RMS velocity components at a distance of 15 mm from the discharge orifice, demonstrate the validity of the FIM-UR injection methodology. The largest differences between the EL and EE approaches appear on the RMS profile of the radial component. The behavior of the Lagrangian particles in the vicinity of the nozzle is certainly altered by the turbulent gas structures, which are not taken into account in the Eulerian FIM-UR model, where a ballistic assumption is used to derive the radial velocity profile. Other differences between EL and EE profiles appear on the center line of the axial velocity component profiles Fig. 15. The entrained air calculated in the Eulerian FIM-UR model only takes into account the air coming from the exterior of the spray. In the EL simulation however, the air entrained by the spray also includes air from the central recirculation zone which reduces the

droplet velocity through drag force. This effect is certainly inaccurate in the vicinity of the injector, where more inertial ligaments and not yet droplets are found.

To sum up, EL and EE simulations accurately capture the spray opening and rotation, as well as particle velocity fluctuations, with no clear advantage for either of both approaches. The observed overall good agreement with experiments for both approaches, especially in the first measurement plane, i.e. close to the injector, indicates that the FIM-UR injection methodology is reasonably accurate for swirling separated flows with pronounced drag effects.

5.2.3. Evaporation and vapor fuel distribution

The use of a single droplet diameter to represent the polydisperse spray shows its limitations in the plots of droplet diameter, Fig. 18. In the experiments a sorting effect is observed, where the largest, most inertial droplets concentrate in the sides of the chamber while the smallest droplets, following the gas flow, are entrained back into the central recirculation zone. If the initial mean droplet diameter is correct (first measurement plane), there seems to be some delay in the sorting effect as small particles appear only after evaporation and are not injected. This tendency is more pronounced in the Eulerian solver, where all particles are stuck on the sidewalls and can not re-enter the central zone (Fig. 13).

The fluctuations of droplet diameter are due to two contributions: the local mean diameter resolved fluctuations, captured in the simulations, and the statistical deviations from the mean diameter due to the local polydispersion of the spray, not accounted for in the simulations. The latter appears to be

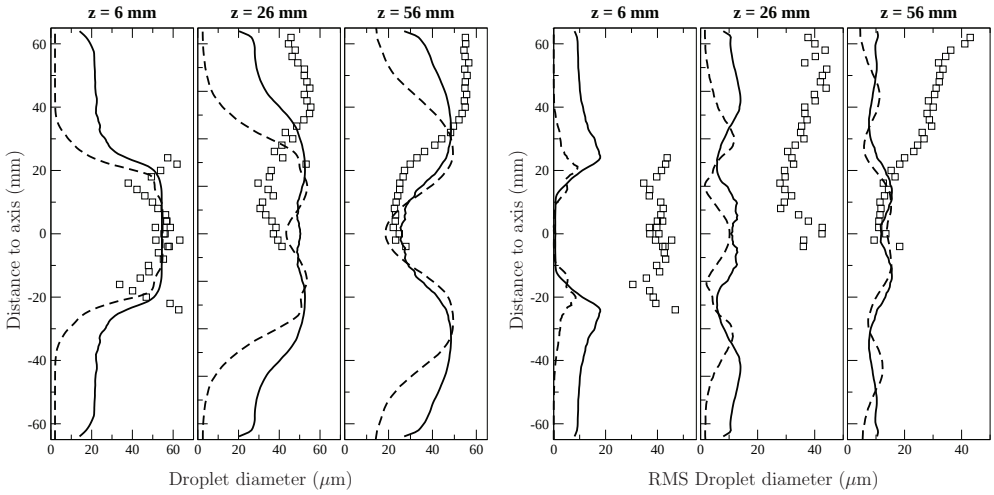

Figure 18: Droplet diameter (Case II). Left: mean, right: RMS. □ PDA, – EL, - - EE

the dominant source of fluctuations in the present configuration, as shown in Fig. 18, right. Note that EL diameter fluctuations are always higher than the EE values, resulting from both the individual history which is naturally taken into account in the Lagrangian formulation and the sampling rate in this area where the particle density is very low.

The resulting fuel vapor mass fraction fields are shown in Fig. 19 for both approaches and appear very similar. The capture of droplets in the corner recirculation zones leads to high fuel vapor mass fraction there and subsequent inhomogeneities through the turbulent mixing with air. Evaporation rate isocontours (4 levels of respectively 3, 6, 9 and 12 $kg/m^3/s$) appear smoother in the EE simulation, due the continuous field approach. This may have an important impact on the flame structure as the resulting evaporated fuel field is slightly more inhomogeneous in the EL than in the EE approach, although the fast and intense turbulent diffusion may reduce this effect.

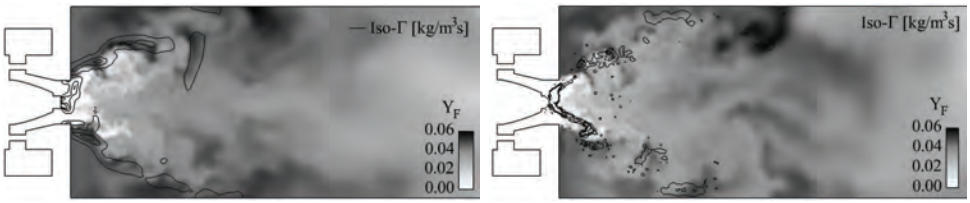

Figure 19: Instantaneous fields of fuel mass fraction in the Mercato chamber (Case II) with isocontours of evaporation rate (4 levels of respectively 3, 6, 9 and 12 $kg/m^3/s$). Comparison between EE (left) and EL(right) at similar instants

6. Conclusions

A methodoloy for fuel injection in combustion chambers, called FIM-UR, was introduced. The methodology is based on geometric and calibration data of pressure-swirl atomizers and models boundary conditions to represent a monodisperse hollow-cone spray for both Lagrangian and Eulerian approaches. The precision of the two different approaches for the modeling of the dispersed phase (Eulerian / Lagrangian) has been investigated in the case of a swirled combustor fed with air and liquid kerosene (Jet-A) operated at ONERA-Fauga. The two approaches were coupled to the same LES gaseous solver AVBP and used identical atomizer parameters which allowed a fair comparison with experimental data.

In a first step, the purely gaseous flow was validated and the observed agreement with the experiments was very good. The compressible LES captured unsteady structures such as the Precessing Vortex Core near the nozzle. A liquid spray was then injected using the FIM-UR boundary conditions. The droplet distribution showed strong inhomogeneities and the PVC was shown to generate unsteady flow-structures on the dispersed phase. Quantitatively, both approaches yielded very similar spray velocity fields, also in

good agreement with the experimental measurements, indicating that the FIM-UR methodology is suitable for swirling flow configurations with pronounced drag effects. Both approaches were able to capture the right opening and rotation of the droplet spray, with no clear advantage for either of both approaches. In terms of fluctuations, both solvers provided reasonable agreement with experiment, although the Eulerian solver suffered from more numerical diffusion.

Due to the monodisperse description of the spray, the mean droplet diameter was not correctly predicted by both approaches, with a more pronounced deviation for the Eulerian solver. The fluctuations of spray mean diameter were underpredicted in the simulations because in the experiments they are mainly due the initial polydispersion of the spray. Although this had limited impact on the spray dynamics, it is crucial for fuel vapor distribution. Work to include polydispersion in both EL and EE formulations is undergoing.

It should also be highlighted that good computational efficiency was obtained for both approaches up to 1024 processors, demonstrating that the two-phase flow LES solver AVBP is well suitable for massively parallel computations.

Acknowledgements

The supports of Turbomeca, of the Délégation Générale de l'Armement, of the European Community through the TIMECOP-AE project (#AST-CT-2006-030828) and Marie Curie Fellowships (contract MEST-CT-2005-020426) are gratefully acknowledged. The simulations have been performed on the cluster IBM BlueGene/P of the Argonne Leadership Computing Fa-

cility. The authors thank the Argonne Leadership Computing Facility at Argonne National Laboratory, which is supported by the Office of Science of the U.S. Department of Energy under contract DE-AC02-06CH11357.

Bibliography

Apte, S., Mahesh, K., Moin, P., 2009. Large-eddy simulation of evaporating spray in a coaxial combustor. Proc. Combust. Inst. 32 (2), 2247–2256.

Apte, S. V., Mahesh, K., Moin, P., Oefelein, J. C., August 2003. Large-eddy simulation of swirling particle-laden flows in a coaxial-jet combustor. Int. J. Multiphase Flow 29 (8), 1311–1331.

Balachandar, S., 2009. A scaling analysis for point-particle approaches to turbulent multiphase flows. Int. J. Multiphase Flow 35 (9), 801–810.

Bayvel, L. P., Orzechowski, Z., 1993. Liquid atomization. Combustion (Hemisphere Publishing Corporation). Taylor & Francis, Washington, USA.

Boileau, M., Pascaud, S., Riber, E., Cuenot, B., Gicquel, L., Poinsot, T., Cazalens, M., 2008a. Investigation of two-fluid methods for large eddy simulation of spray combustion in gas turbines. Flow, Turb. Combust. 80 (3), 291–321.

Boileau, M., Staffelbach, G., Cuenot, B., Poinsot, T., Bérat, C., July 2008b. LES of an ignition sequence in a gas turbine engine. Combust. Flame 154 (1-2), 2–22.

Boivin, M., Simonin, O., Squires, K. D., 2000. On the prediction of gas-solid flows with two-way coupling using large eddy simulation. Phys. Fluids 12 (8), 2080–2090.

Colin, O., Rudgyard, M., 2000. Development of high-order Taylor-Galerkin schemes for unsteady calculations. J. Comput. Phys. 162 (2), 338–371.

Cossali, G., 2001. An integral model for gas entrainment into full cone sprays. J. Fluid Mech. 439, 353–366.

Dagaut, P., Cathonnet, M., 2006. The ignition, oxidation, and combustion of kerosene: A review of experimental and kinetic modeling. Prog. Energy Combust. Sci. 32 (1), 48–92.

Desjardins, O., Moureau, V., Pitsch, H., 2008. An accurate conservative level set/ghost fluid method for simulating turbulent atomization. J. Comput. Phys. 227, 8395–8416.

Dombrowski, N., Johns, W. R., 1963. The Aerodynamic Instability and disintegration of liquid sheets. Chem. Eng. Sci. 18, 203–214.

Elghobashi, S., 1994. On predicting particle-laden turbulent flows. Appl. Sci. Res. 52, 309–329.

Février, P., Simonin, O., Squires, K., 2005. Partitioning of particle velocities in gas-solid turbulent flows into a continuous field and a spatially uncorrelated random distribution: Theoretical formalism and numerical study. J. Fluid Mech. 533, 1–46.

Fraser, R. P., Dombrowski, N., Routley, J. H., 1963. The Atomisation of a liquid sheet by an impinging air stream. Chem. Eng. Sci. 18, 339–353.

Frössling, N., 1938. Über die Verdunstung fallender Tropfen (On the evaporation of falling drops). Gerlands Beitr. Geophys. 52, 170–216.

García-Rosa, N., July 2008. Phénomènes d'allumage d'un foyer de turbomachine en conditions de haute altitude. Ph.D. thesis, Université de Toulouse - Ecole doctorale : Mécanique, Energétique, Génie civil, Procédés, Toulouse, France.

Gradshteyn, I. S., Ryzhik, I. M., June 1980. Table of Integrals, Series and Products, 2nd Edition. Academic Press Inc.

Harstad, K., Bellan, J., 2004. Modeling evaporation of jet a, jp-7, and rp-1 drops at 1 to 15 bars. Combust. Flame 137 (1-2), 163–177.

Hirschfelder, J. O., Curtiss, F., Bird, R. B., 1964. Molecular theory of gases and liquids, 2nd Edition. John Wiley & Sons, New York.

Hubbard, G. L., Denny, V. E., Mills, A. F., 1975. Droplet evaporation: effects of transient and variable properties. Int. J. Heat Mass Transf. 18, 1003–1008.

Jones, W. P., Whitelaw, J. H., 1982. Calculation methods for reacting turbulent flows: a review. Combustion and Flame 48, 1–26.

Kaufmann, A., Moreau, M., Simonin, O., Hélie, J., 2008. Comparison between Lagrangian and mesoscopic Eulerian modelling approaches for iner-

tial particles suspended in decaying isotropic turbulence. J. Comput. Phys. 227 (13), 6448–6472.

Kuo, K. K., 2005. Principles of Combustion, 2nd Edition. Wiley-Interscience, New York.

Lamarque, N., 2007. Schémas numériques et conditions limites pour la simulation aux grandes échelles de la combustion diphasique dans les foyers d'hélicoptère. Phd thesis, INP Toulouse.

Lee, C. H., Reitz, R. D., 1999. Modelling the effect of gas density on the drop trajectory and breakup size of high speed liquid drops. Atomization Sprays 9, 497–517.

Lefebvre, A. H., 1989. Atomization and Sprays. Combustion (Hemisphere Publishing Corporation). Taylor & Francis.

Lucca-Negro, O., O'Doherty, T., 2001. Vortex breakdown: a review. Prog. Energy Combust. Sci. 27, 431–481.

Luche, J., 2003. Elaboration of reduced kinetic models of combustion. application to a kerosene mechanism. Ph.D. thesis, LCSR Orleans.

Mahesh, K., Constantinescu, G., Moin, P., 2004. A numerical method for large-eddy simulation in complex geometries. J. Comput. Phys. 197 (1), 215–240.

Menard, T., Tanguy, S., Berlemont, A., 2007. Coupling level set/vof/ghost fluid methods: Validation and application to 3d simulation of the primary break-up of a liquid jet. Int. J. Multiphase Flow 33, 510–524.

Moreau, M., Simonin, O., Bédat, B., March 2010. Development of gas-particle Euler-Euler LES approach: A priori analysis of particle sub-grid models in homogeneous isotropic turbulence. Flow, Turb. Combust. 84 (2), 295–324.

Nicoud, F., Ducros, F., 1999. Subgrid-scale stress modelling based on the square of the velocity gradient. Flow, Turb. Combust. 62 (3), 183–200.

Patel, N., Menon, S., 2008. Simulation of spray–turbulence–flame interactions in a lean direct injection combustor. Combust. Flame 153 (1-2), 228–257.

Poinsot, T., Lele, S., 1992. Boundary conditions for direct simulations of compressible viscous flows. J. Comput. Phys. 101 (1), 104–129.

Poinsot, T., Veynante, D., 2001. Theor. Numer. Combust. R.T. Edwards.

Pope, S. B., 2000. Turbulent Flows. Cambridge University Press.

Prosperi, B., Delay, G., Bazile, R., Helie, J., Nuglish, H., 2007. FPIV Study of gas entrainment by a hollow cone spray submitted to variable density. Exp. Fluids 43 (2), 315–327.

Riber, E., 2007. Développement de la méthode de simulation aux grandes échelles pour les écoulements diphasiques turbulents. Phd thesis, INP Toulouse.

Riber, E., Moureau, V., García., M., Poinsot, T., Simonin, O., 2009. Evaluation of numerical strategies for LES of two-phase reacting flows. J. Comput. Phys. 228 (2), 539–564.

Rizk, N. K., Lefebvre, A. H., 1980. Influence of liquid film thickness on airblast atomization. J. Eng. Gas Turbines Power 102, 706–710.

Rizk, N. K., Lefebvre, A. H., Aug. 1983. Influence of atomizer design features on mean drop size. Am. Inst. Aeronaut. Astronaut. J. 21 (8), 1139–1142.

Rizk, N. K., Lefebvre, A. H., May-June 1985. Internal Flow Characteristics of simplex swirl atomizers. J. Propuls. Power 1 (3), 193–199.

Saffman, P., 1973. On the settling speed of free and fixed suspensions. Studies Appl. Math. 52 (2), 115–127.

Sakiz, M., Simonin, O., July 1998. Numerical experiments and modelling of non-equilibrium effects in dilute granular flows. In: Cépaduès (Ed.), Proceedings of the 21st International Symposium on Rarefied Gas Dynamics. Vol. 1. pp. 287–294.

Sankaran, V., Menon, S., 2002. Les of spray combustion in swirling flows. J. Turb. 3, 011.

Schiller, L., Naumann, A., 1933. Uber die grundlegenden Berechnungen bei der Schwerkraftaufbereitung. Ztg. Ver. Deut. Ing. 77, 318–320.

Selle, L., Lartigue, G., Poinsot, T., Koch, R., Schildmacher, K.-U., Krebs, W., Prade, B., Kaufmann, P., Veynante, D., 2004. Compressible large-eddy simulation of turbulent combustion in complex geometry on unstructured meshes. Combust. Flame 137 (4), 489–505.

Simonin, O., 1996. Combustion and turbulence in two phase flows. Lecture Series 1996-02, Von Karman Institute for Fluid Dynamics.

Simonin, O., Fevrier, P., Lavieville, J., 2002. On the spatial distribution of heavy particle velocities in turbulent flow: from continuous field to particulate chaos. J. Turb. 3, N40.

Sirignano, W. A., 1999. Fluid dynamics and transport of droplets and sprays. Cambridge University Press.

Smagorinsky, J., 1963. General circulation experiments with the primitive equations: 1. the basic experiment. Mon. Weather Rev. 91, 99–164.

Squires, K. D., Eaton, J. K., 1991. Preferential concentration of particles by turbulence. Phys. Fluids 3 (5), 1169–1178.

Taylor, G., 1948. The mechanics of swirl atomizer. In: 7th International Congress on Applied Mechanics. Vol. 2. pp. 280–285.

Vié, A., Sanjosé, M., Jay, S., Angelberger, C., Cuenot, B., Massot, M., 2010. Evaluation of a Multifluid Mesoscopic Eulerian Formalism on the Large Eddy Simulation of an aeronautical-type configuration. In: 7th International Conference on Multiphase Flow. May 30 - June 4, Tampa, US.

A. Model for air entrainment by a hollow-cone spray

The FIM-UR methodology requires the evaluation of air entrainment, and more specifically the values of R_i, $\dot{m}_a$ and $J_{s,l}\left(x_0, x_i\right)$. Cossali (2001) proposed a model for the air entrainement coefficient Λ for full cone sprays, measuring the mass flow rate of the air entrained per unit distance from the discharge orifice. This model is first recalled below, then extended to hollow cone sprays.

A.1. Integral model for gas entrainment by full-cone sprays

Limiting solutions of the gas entrainment equation in the near and far-field of the injector nozzle have been derived from conservative balances of the air/liquid mixture. They provide the entrained mass flow rate by the spray as a function of the mass flow rate of the injected liquid, the gas properties, the mean drop size and the axial distance from the discharge orifice. The main hypotheses used by Cossali (2001) are listed below:

A1 The liquid spray is injected into a quiescent atmosphere at uniform pressure: in gas-turbine combustion chambers, the atomizer is usually located on the axis of the gas recirculation zone, ensuring that the gas is almost quiescent at this location.

A2 The model is derived for a pressurized atomizer producing a full-cone spray pattern.

A3 The liquid and gas phases are in steady state.

A4 The liquid is non-evaporating, and the momentum exchange between phases is reduced to the total drag force on all spray droplets.

A5 The drag force applied in the model is the aerodynamic drag on spherical particle.

A6 The profiles of liquid and gas velocity, as wall as droplet number density are self-similar.

A.2. Definition of self-similarity profiles for the integral model for gas entrainment into hollow-cone sprays

To meet assumption **A6** for hollow-cone sprays, self-similarity profiles must be defined. The non-dimensional coordinate (Pope, 2000) ξ is now:

$$\xi = \frac{r}{R_S(x)} = \frac{r}{R_S^0 + (x - x_0)\tan\theta_S} \tag{A.1}$$

where θ_S is the half spray angle. Assuming self-similarity of gas mean axial velocity $u_{g,x}$, liquid mean axial velocity $u_{l,x}$ and volume fraction profiles α_l, they may be written in the form (Cossali, 2001):

$$u_{g,x}(r,x) = W(x)\ f(\xi) \tag{A.2}$$

$$u_{l,x}(r,x) = U(x)\ f(\xi) \tag{A.3}$$

$$\alpha_l(r,x) = N(x)\ \varphi(\xi) \tag{A.4}$$

introducing two similarity functions f and φ and where the functions W, U and N describe the axial variation of the amplitudes.

For the velocity, the similarity profile f corresponds to a turbulent round jet in a quiescent atmosphere:

$$f(\xi) = \frac{1}{(1 + a\,\xi^2)^2} \tag{A.5}$$

where a is defined so that the jet's half width is located on the (Ox') axis, i.e. $f(1) = 1/2$. Then $a = \sqrt{2} - 1$.

For the liquid volume fraction, the similarity profile φ is defined so as to be minimum at the centerline:

$$\varphi(\xi) = \frac{b\,\xi^2}{(1 + c\,\xi^2)^4} \tag{A.6}$$

The parameters b and c are defined to ensure first - that the maximal value of the φ function is 1, and secondly - that this maximum is located on the (Ox') axis, i.e. $\varphi(1) = 1$. This leads to $c = 1/3$ and $b = 256/81$ (Fig. A.20).

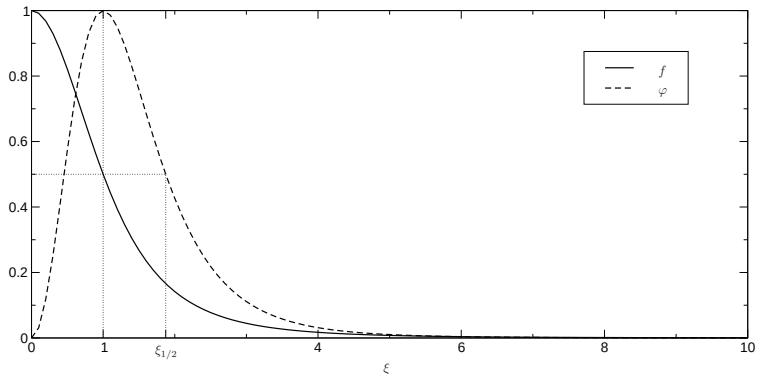

Figure A.20: Similarity functions f and φ as functions of ξ.

The radius of the injection external boundary R_i in the plane $x = x_i$ must be equal or larger than the position $\xi_{1/2}$ of the half-width of the φ function:

$$R_i \geq \xi_{1/2}\, R_S^i \tag{A.7}$$

$$\text{where: } \varphi\left(\xi_{1/2}\right) = \frac{1}{2} \text{ i.e. } \xi_{1/2} = 1.87397 \tag{A.8}$$

A.3. Evaluation of the air entrainment coefficient

The entrained air $\dot{m}_a$ is related to the liquid flow rate and to the distance from the discharge orifice through the air entrainment coefficient $\Lambda(x)$: $\dot{m}_a(x) = \Lambda(x)\ \dot{m}_l\ (x - x_0)/2R_0$. The entrainment coefficient is given in the near field of the injector nozzle by (Cossali, 2001):

$$\Lambda(x) \;=\; H_0 \left(\frac{2R_0\,\mu}{\dot{m}_l}\right)^{1/6} \left(\frac{\rho}{\rho_l}\right)^{5/6} \left(\frac{2R_0}{d}\right)^{2/3} \left(\frac{x - x_0}{2R_0}\right)^{1/2} \tag{A.9}$$

$$\text{where:} \quad H_0 = \sqrt{3}\left(\frac{4}{\pi}\right)^{1/3}\left(\frac{2\pi\, Q^2\, R\, {C_M}^{2/3}}{M\, B^{1/3}\, C^{2/3}}\right)^{1/2} \tag{A.10}$$

$$\text{and: } \dot{m}_a\left(x_0\right) = 0 \tag{A.11}$$

The quantities Q, M, B, C, and R have to be calculated by integration of the functions f and φ. Their expression derived in Cossali (2001) are recalled in Eqs. A.12 to A.16. To obtain the integrals B, C and R, the formula (3.197.1) p. 314 of Gradshteyn and Ryzhik (1980) has been used. ${}_2F1$ stands for the first Gauss hypergeometric function, tabulated in Tab. A.6.

$$\text{gas flow-rate} \qquad Q = \int_0^\infty f(\xi)\xi d\xi = \frac{1}{2\left(\sqrt{2}-1\right)} \tag{A.12}$$

$$\text{gas momentum flux} \qquad M = \int_0^\infty f^2(\xi)\xi d\xi = \frac{1}{6\left(\sqrt{2}-1\right)} \tag{A.13}$$

$$\text{liquid flow-rate} \qquad B = \int_0^\infty f(\xi)\varphi(\xi)\xi d\xi = \frac{32}{45}\,{}_2F1\left(2,2;6;4-3\sqrt{2}\right) \tag{A.14}$$

$$\text{liquid momentum flux} \qquad C = \int_0^\infty f^2(\xi)\,\varphi(\xi)\xi d\xi = \frac{64}{189}\,{}_2F1\left(4,2;8;4-3\sqrt{2}\right) \tag{A.15}$$

$$\text{drag force}^1 \qquad R = \int_0^\infty f(\xi)|f(\xi)|^{2/3}\varphi(\xi)\xi d\xi = \frac{8}{19}\,{}_2F1\left(\frac{10}{3},2;\frac{22}{3};4-3\sqrt{2}\right) \tag{A.16}$$

The coefficient C_M is calculated from the discharge-orifice values $u^0_{l,x}$ and

[1]The exponent value of 2/3 comes from the correction part of Lee and Reitz (1999) for the Stokes drag. The 2/3 coefficient is preferred to the close value 0.687 of the Schiller and Naumann (1933)'s correction, as it leads to an analytical antiderivative function.

${}_2F1\left(2,2;6;4-3\sqrt{2}\right)$	0.85998
${}_2F1\left(4,2;8;4-3\sqrt{2}\right)$	0.79844
${}_2F1\left(\frac{10}{3},2;\frac{22}{3};4-3\sqrt{2}\right)$	0.81465

Table A.6: Tabulated values for ${}_2F1$.

α_l^0 defined in Eqs. (40) and (41):

$$C_M = \frac{R_0^2 \int_0^{R_0} \left[\alpha_l^0(r_0)\, u_{l,x}^0(r_0)\right]^2 r_0\, dr_0}{2\left(\int_0^{R_0} \alpha_l^0(r_0)\, u_{l,x}^0(r_0)\, r_0\, dr_0\right)^2} = \frac{1}{1-X} \tag{A.17}$$

The expression of Eq. (A.9) can now be used to obtain the K_a coefficient required for the injection model in Eq. (59):

$$K_a = H_0 \left(\frac{2R_0\,\mu}{\dot{m}_l}\right)^{1/6} \left(\frac{2R_0}{d}\right)^{2/3} \frac{\dot{m}_l}{(2R_0)^{3/2}\,{\rho_l}^{5/6}} \tag{A.18}$$

Moreover, the momentum exchange term $J_{s,l}\,(x_0, x_i)$ used in Eq. 52 is also evaluated from the air entrainment coefficient as (Cossali, 2001):

$$J_{s,l}\,(x_0, x_i) = -\Lambda^2\,(x_i)\,\frac{\dot{m}_l^2\, M}{8\pi {R_0}^2\,\rho\, Q^2} \tag{A.19}$$

These two last expressions allow to close the system for the determination of the boundary profiles in the (EE) approach. Equation 52 becomes:

$$u_{l,x}^i|_{mean} = \frac{\dot{m}_l}{\pi R_0^2}\, A_u \tag{A.20}$$

with the constant A_u given by:

$$A_u \;=\; \frac{C_M}{\rho_l} - \frac{M\,\Lambda^2\,(x_i)}{8\,\rho Q^2} \tag{A.21}$$